Journal of Materials Chemistry C

ROYAL SOCIETY OF CHEMISTRY

PAPER

View Article Online
View Journal | View Issue

Cite this: J. Mater. Chem. C, 2021, 9, 657

Enhancing NIR emission in $ZnAl_2O_4$:Nd,Ce nanofibers by co-doping with Ce and Nd: a promising biomarker material with low cytotoxicity†

Rocío Estefanía Rojas-Hernandez, *[a] Fernando Rubio-Marcos, [bc] Giulio Gorni, [d] Carlo Marini,[d] Mati Danilson, [e] Laura Pascual,[f] Rodrigo Uchida Ichikawa,[g] Irina Hussainova [a] and José Francisco Fernandez [b]

Received 7th October 2020,
Accepted 23rd November 2020

DOI: 10.1039/d0tc04752j

rsc.li/materials-c

Development of new near infrared luminescent (NIR) emitters improves our understanding of their fundamental structure–property relationships. The ability to use efficient energy transfer to convert ultraviolet or visible light photons to enhance the NIR emission has attracted a great deal of attention in down-conversion applications. Taking advantage of the sol–gel impregnation process and growth of materials along a support or template, core–shell structured nanofibers of $ZnAl_2O_4$ – based ceramic doped with cerium and neodymium were synthesized with the help of an elaborate facile and cost-efficient strategy. The color-tunable emissions make this material a suitable host for a wide range of applications, *e.g.*, bio-imaging, security markers, imaging devices, optical coatings, and solar cells. This research correlates the defects and the remarkable optical properties of the developed structures. Specified conditions of sol–gel processing combined with the incorporation of rare-earth elements in various concentrations provide the possibility of tuning the ratio between Ce^{3+} and Ce^{4+} in the nanofibers with an average diameter of 50 nm and, therefore, their functional response. It is important to clarify the role of trivalent and tetravalent cerium cations in the modulation of NIR emission to establish the luminescence mechanism. The NIR emitter luminescent compound $ZnAl_2O_4$:Nd,Ce, which adopts a spinel-type structure, is studied using the X-ray absorption near-edge structure technique. For the first time, this study reveals the energy transfer from Ce^{3+} to Nd^{3+} and the enhancement of the NIR emission due to the presence of Ce^{4+} in the $ZnAl_2O_4$:Nd,Ce spinel compound. Cytotoxicity analyses suggest the viability of the synthesized nanofibers, which opens new avenues in bio-imaging applications.

Introduction

Spinel-type phosphors provide an attractive platform to study how the local structure around the luminescence centers influences the final luminescence response. $ZnAl_2O_4$ based spinel compounds have been extensively studied and used in different applications such as catalytic supports or as an active material for automobile catalysis, as a transparent conductive oxide, sintering aid and as a photo-catalytic material.[1] $ZnAl_2O_4$ can be used as a blue or green pigment upon doping with cobalt or nickel. Besides, $ZnAl_2O_4$ is an appropriate host for luminescence due to the transparency to wavelengths >320 nm, that promotes its use in lighting, and optoelectronic devices in the VIS-NIR region and as a potential material to meet the requirements of mid-infrared (MIR) optoelectronic devices or electroluminescent displays.[2,3] The luminescence of $ZnAl_2O_4$ doped with Cr^{3+} has been reported[4] as well as the luminescence obtained by doping with rare earth (RE) elements such as Eu, Tb, and Er/Yb cations.[5–7] RE based materials exhibit high photostability, high luminescence quantum yield, and sharp emission bands, providing more selectivity for testing. Recent studies also showed blue and white luminescence in the pure $ZnAl_2O_4$ phase.[8–10] However, there is a lack of evidence to determine which defect centers are responsible for such emissions in an undoped matrix.

[a] Department of Mechanical and Industrial Engineering, Tallinn University of Technology, Ehitajate 5, 19180 Tallinn, Estonia. E-mail: rocio.rojas@taltech.ee
[b] Electroceramic Department, Instituto de Cerámica y Vidrio, CSIC, Kelsen 5, 28049, Madrid, Spain
[c] Escuela Politécnica Superior, Universidad Antonio de Nebrija, C/Pirineos, 55, 28040, Madrid, Spain
[d] CELLS – ALBA Synchrotron Radiation Facility, Carrer de la Llum 2-26, Cerdanyola del Valles, 08290, Barcelona, Spain
[e] Department of Material and Environmental Technology, Tallinn University of Technology, Ehitajate 5, 19180 Tallinn, Estonia
[f] Instituto de Catálisis y Petroleoquímica CSIC, ICP-CSIC, C/Marie Curie 2, 28049, Madrid, Spain
[g] Instituto de Pesquisas Energéticas e Nucleares, IPEN/CNEN, Av. Lineu Prestes, 2242, 05508-000, São Paulo, SP, Brazil

† Electronic supplementary information (ESI) available. See DOI: 10.1039/d0tc04752j

During the past few decades, the study of near-infrared (NIR) emission has attracted a lot of attention due to its potential applications in the biological, optical, and solar energy fields. In the case of $ZnAl_2O_4$, the NIR emission is scarce, and only one study has addressed the luminescence of Nd^{3+}, where NIR emission was demonstrated at 905 nm, 1064 nm and 1335 nm under 808 nm excitation.[11] At the same time, a considerable amount of effort has been devoted to enhancing the luminescence response from the far UV to NIR range; different approaches can be addressed such as the employment of plasmonic particles, dye sensitization, alteration of the crystal field, construction of a core–shell structure, RE sensitization, donor sensitization through the matrix, *etc.*[12–16] In particular, the employment of a RE sensitizer has been mainly adopted to solve the spectral mismatch of crystalline silicon-based technology and the solar spectrum to improve the response in optical amplifiers and biomedical applications, through the up-conversion or down-conversion process. In particular, for NIR emission, the sensitizer should fulfill some requirements such that it should have an intense broadband absorption and its emission must be in the region corresponding to twice the energy of the cation selected to emit in the NIR range. The most promising systems for downconversion rely on lanthanide cations (RE). Considering the energy levels of Nd^{3+}, as shown in the Dieke energy level diagram[17] the energy level structure of Nd^{3+} has an excited state at 880 nm above the ground state. Therefore, the characteristic transition between Nd^{3+} energy levels corresponding to the emission around 900 nm ($^4F_{3/2} \rightarrow {}^4I_{9/2}$), 1070 nm ($^4F_{3/2} \rightarrow {}^4I_{11/2}$), and 1330 nm ($^4F_{3/2} \rightarrow {}^4I_{13/2}$) is achieved, under 880 nm excitation, as well with 808, 750 and 583 nm (strong absorptions bands of Nd^{3+}). Nevertheless, direct excitation in the VUV range is quite weak due to the rich energy level structure of Nd^{3+} cations and their lower absorption cross-section. In order to increase the NIR emission a self-activated host matrix or quantum cutting or down conversion by suitable co-doping has been proposed.[18–21] Ce^{3+}, Eu^{2+}, Sm^{2+}, and Yb^{2+} exhibit intense excitation due to the f–d transitions as well as the excitation bands in the UV-blue region. Generally, divalent and trivalent cations are the most used due to their strong f–d transitions. However, tetravalent lanthanides such as Ce, Tb and Pr exhibit strong absorption in the nUV region due to charge transfer transitions and their use has not been fully exploited.[22] There is a lack of in-depth study of the Ce/Nd pair. Yamaga *et al.*[23] observed luminescence peaks of Nd^{3+} for Nd:Ce:YAG ceramics under 354 nm excitation; these lines do not appear in the single doped samples with Nd, indicating that Ce^{3+} plays an energy transfer role. The enhancement of NIR emission in YAG ceramics was also described by Samuel *et al.*,[24] concluding that Ce ions are advantageous as a co-dopant to Nd:YAG ceramics to achieve more efficient IR emission. The energy transfer from Ce^{3+} to Nd^{3+} was also observed in $Ca_xSr_{1-x}S:Ce^{3+},Nd^{3+}$ phosphors. However, these studies do not specify the role of Ce^{3+} or Ce^{4+} in the host. On the other hand, Vyas *et al.*,[25] studied the NIR emission resulting from the $Ce^{4+} \rightarrow Yb^{3+}/Nd^{3+}$ energy transfer in the K_2CeO_3 host, which was attributed to the broad band in the absorption spectrum due to the charge transfer absorption of Ce^{4+}. Similar results were observed for the Li_2CeO_3 host where a broad excitation band around 400 nm was a feature of a charge transfer state (CTS) of Ce^{4+}, and the NIR emission at 1088 nm was observed when the host is doped with Nd^{3+}.[26] Thus, it was stated that the energy transfer from the Ce^{4+}–O^{2-} state can populate ^4D_j levels of Nd^{3+}, following which Nd^{3+} can reach the $^4F_{3/2}$ state through several steps that involve the generation of phonons, and finally, a radiative transition occurs from this state to $^4I_{9/2}$, $^4I_{11/2}$, and $^4I_{13/2}$ states. In particular, for Ce, there is a first allowed charge transfer band of Ce^{4+} due to the transition $\pi t_{1g} \rightarrow f$.[22] Jogerson[27] presented the theory of Ce transition pointing to the fact that the absorption bands of cerium in the trivalent state are 2 times narrower than the electron-transfer bands of cerium in its tetravalent state. These assumptions corroborate the higher absorption due to the charge transfer band of Ce^{4+}. From inspection of the Dieke's diagram and taking into account the previous assumptions, the potential couple Nd/Ce was chosen in this study to functionalize the $ZnAl_2O_4$ spinel-type structure.

As there is an apparent relationship between the luminescence center and the local structure surrounding, it is of obvious importance to study in-depth their presence on the $ZnAl_2O_4$ structure. $ZnAl_2O_4$, also called gahnite, has a spinel structure belonging to the *Fd3m* space group and can have a direct or an inverse structure. In the direct structure, the Zn^{2+} cations occupy the tetrahedral sites while the Al^{3+} cations occupy the octahedral sites.[28] In the inverse spinel structure, a proportion of Zn^{2+} and Al^{3+} cations are in the octahedral sites and tetrahedral sites, respectively. This proportion is called the inversion rate.

Besides, to obtain phosphors with enough luminescence response, the process of synthesis usually requires high temperatures for annealing. For this reason, most of the systems are prepared by a conventional solid-state synthesis or a wet-chemical technique followed by an annealing process, which usually results in large size distribution, irregular morphology, and aggregated particles. These methods do not allow fine control of the particle morphology, which is a limiting factor for their potential applications. For this reason, it is important to find a suitable method to prepare luminescent nanostructures with a high degree of uniformity.

An alternative approach is the synthesis of nanofibers, which is becoming more widely recognized due to the feasibility to join different properties arising from the size, structure, porosity, and their assembly.[29] Nanofibers have been synthesized by different methods such as electrospinning, self-assembly, phase separation, and template synthesis, representing the morphology of a potential characteristic to be used in a wide range of applications such as filtration, sensors, composite materials, textiles, bio-imaging, light-emitting diodes, *etc.* Most of these methods are generally of laboratory scale, so the efforts should be concentrated on development of a scalable process for industries. Moreover, these methods usually produce long and continuos fibers that are not suitable for production of short fibers directly, which are beneficial for some applications. To break up the long fibers, post-spinning processes or modification to the electrospinning setup is required.[30] The process presented here is one of the most preferred methods for the nanofiber production due to the reduction of the additional processing steps as the ultrasonication process creates smaller pieces out of ultralong fibers. In particular, for zinc aluminate based materials, the

synthesis of nanofibers is quite limited; the ultra-long nanofibers of $ZnAl_2O_4$ doped with Nd^{3+} and an average diameter of 450 nm have been synthesized using the electrospinning technique.[31] The morphology can be tuned from nanofibers to nanoparticles by changing the degree of polymerization of PVP. The photoluminescence response is obtained in the 700–100 nm range, demonstrating the main emission peak at 1064 nm under 808 nm excitation.[11] Ceramic nanofibers with an average diameter of 160 nm and composed of ZnO, Al_2O_3, and $ZnAl_2O_4$ phases were produced by electrospinning and used as a photocatalyst for the conversion of CO_2.[32]

Herein, we report a novel strategy for NIR emitters based on $ZnAl_2O_4$:Nd,Ce nanofibers. The impregnation carried out through the sol–gel route on gamma-alumina nanofibers as templates serves to provide the desired nanofiber morphology. Moreover, the procedure allows the functionalization of short nanofibers fragments by doping. For the first time, $ZnAl_2O_4$ homogeneous and well-dispersed nanofibers were synthesized. The study follows the kinetics of the reaction of a sol–gel based method and opens the evaluation of the concentrations of the RE couple to enhance the luminescence performance. As expected the Ce enhances the NIR luminescence.

Materials & methods

Materials

For the preparation of $ZnAl_2O_4$:Nd,Ce nanofibers, γ-Al_2O_3 nanofibers, $Zn(NO_3)_2{\cdot}6H_2O$ (zinc nitrate hexahydrate, Sigma Aldrich, reagent grade, 98%), $Ce(NO_3)_3{\cdot}6H_2O$ (cerium c nitrate hexahydrate, Sigma Aldrich, reagent grade, 98%), and Nd_2O_3 (Metall Rare Earth Limited, 99.5%), were used as precursors, distilled water was used as a solvent and HNO_3 (Sigma Aldrich, 65%) was used as a catalyst. The samples prepared had the nominal composition (in mol%); henceforth, all compositions in this paper are expressed in mol%.

Synthesis

As a first step, the hydrolysis of $Zn(NO_3)_2{\cdot}6H_2O$ was initiated by preparing a solution (solution A) composed of $Zn(NO_3)_2{\cdot}6H_2O$ and water. After mixing, the solution was stirred at RT for 20 min. A separate solution of cerium nitrate was prepared by dissolving the required amount of nitrate in water (solution B). Nd_2O_3 was dissolved in nitric acid HNO_3 (Sigma-Aldrich, 65%) to form nitrate solution (solution C). The last two solutions, B and C, were added slowly to solution A while stirring. This solution was added dropwise onto the γ-Al_2O_3 nanofibers and stirred for 30 min. After this stage the final solution was sonicated using an UP200Ht, Hielscher to disperse homogeneously the nanofibers. Due to the cavitation created during the sonication process, nanofibers deagglomerate. The studied compositions are as follows: $ZnAl_2O_4$:xNd,yCe (x = 0.02 and y = 0.02, 0.04, and 0.06 mol%) doped only with Nd and co-doped with different Ce doping concentrations and annealed at 1200 °C for 2 hours in air.

Structural and microstructural characterization

The crystalline phases were characterized by analysing X-ray diffraction (XRD) data collected using a Rigaku SmartLab SE with a D/teX Ultra 250 1D detector. The X-ray source is a copper sealed 2 kW tube target producing Cu Kα and Kβ emission lines from a generator in this case operating at 40 kV. The measurements were performed at room temperature from 10 to 110° (2θ) with a 0.01° step with 10 seconds per step to optimize the application of Rietveld refinement.[33,34] The refinements were performed using TOPAS 6 software.

Raman spectroscopy was carried out using a confocal Raman microscopy instrument (Witec ALPHA 300RA) with a Nd:YAG laser excitation at 532 nm at RT and a 100× objective lens (NA = 0.95). The incident laser power was 0.171 mW. The optical diffraction resolution of the confocal microscope was limited to about ~230 nm laterally. Raman spectral resolution of the system is down to 0.02 cm^{-1}, under the best measurements conditions. The microscopy sample was mounted in a piezo-driven scan platform having a 4 nm lateral accuracy. The collected spectra were processed and analyzed by using Witec Control Plus software 2.08.

For microstructural characterization of the nanofibers, a field emission scanning electron microscope (FE-SEM Zeiss ULTRA-55, Germany) equipped with an EDS (energy dispersive X-ray spectrometer, BRUKER, Esprit 1.82 system, USA) with a voltage of up to 20 kV and magnification up to 50k× was used. In addition, the detailed morphology and crystal structure of the sample were evaluated using a 200 kV (TEM/STEM) JEOL 2100F transmission electron microscope equipped with a field emission electron gun giving a point resolution of 0.19 nm. EDX analysis was performed with an X-Max80 detector (Oxford Instruments) attached to the equipment. For TEM sample preparation, the particles were carefully suspended in ethanol and dispersed using an ultra-sonication bath for 10 minutes. A drop of the suspension was deposited on a conventional lacey carbon copper TEM grid. After the evaporation of ethanol, the particles were retained at the grid.

X-ray absorption near-edge structure spectroscopy (XANES) and extended X-ray absorption fine structure spectroscopy (EXAFS) were carried out at Ce L_3-edge, Nd L_2-edge and Zn K-edge at the CLAESS beamline of the ALBA synchrotron facility. The spectra at Ce and Nd L-edge were collected in fluorescence mode on pellets placed at 45° incidence and the fluorescence signal was measured using a 6-channel silicon drift detector (SDD) Xspress3 from Quantum Detector. For Zn K-edge, the pellets were measured in transmission mode by diluting a suitable amount of sample in cellulose and the incident and transmitted signal measured by two ionization chambers. All the measurements were performed at room temperature (RT). The final spectra represent an average of at least three XAS scans. The X-ray absorption data were analyzed using ATHENA and ARTHEMIS software.[35]

X-ray photoelectron spectroscopy (XPS) was carried out with the help of a Kratos Analytical Axis Ultra DLD spectrometer equipped with a monochromatic Al Kα X-ray source and an achromatic Mg Kα/Al Kα dual anode X-ray source. The monochromatic Al Kα anode (1486.6 eV) was operated at 150 W and 15 kV. The 180° hemispherical energy analyzer with an average radius of 165 mm was operated using a hybrid lens mode at a pass energy of 160 eV for survey spectra and 20 eV for region spectra. XPS spectra were recorded at a take-off angle of 90° from the surface of the sample holder using an aperture slot of 300 × 700 μm^2. Samples were

mounted on a stainless-steel sample bar (130 × 15 mm^2). The relative atomic concentrations of the elements were determined from the appropriate integrated peak areas at the core level and the sensitivity factors provided by the original analysis Kratos Vision 2.2.10 software. The Shirley background subtraction was used to calculate the relative atomic concentrations.

Optical characterization

The UV-VIS-NIR was performed using a PerkinElmer LAMBDA 1050 UV-VIS-NIR spectrophotometer. The luminescence properties of these materials were examined by recording the emission spectra. The photoluminescence (PL) spectra of the phosphor particles were recorded with a spectrofluorometer (Fluorolog®-3, HORIBA Jobin Yvon) at RT. The emission spectrum was recorded over the wavelength range of 830–1400 nm, using a xenon arc lamp as the excitation source (λ_{exc} = 825 and 359 nm).

Cytotoxicity assays

The tumor epithelial cell line HeLa (cervix adenocarcinoma) was used in this study for cytotoxicity analysis. HeLa cells were grown in Dulbecco's modified Eagle's medium (DMEM) supplemented with 10% (v/v) fetal bovine serum (FBS), 50 units per mL penicillin and 50 μg mL^{-1} streptomycin. Cell cultures were performed in a 5% CO_2 atmosphere at 37 °C and maintained in a Steri-Cult 2000 incubator (Hucoa-Erloss, Madrid, Spain). The cells were seeded at 24-multiwell dishes (Falcon, St. Louis, MO, USA). Experiments were performed with cells at 60–70% of confluence.

A suspension of $ZnAl_2O_4$ was prepared in phosphate buffered saline (PBS). Then, $ZnAl_2O_4$ suspensions with solid concentrations of 1, 10 and 100 μg mL^{-1} were prepared in DMEM from the suspension in PBS. Cells were incubated for 24 h with appropriate concentrations of $ZnAl_2O_4$. After incubation, cells were washed three times with PBS and incubated again with DMEM for 24 h. Finally, the cell viability was determined after treatments using 3-(4,5-dimethylthiazol-2-yl)-2,5-diphenyltetrazolium bromide, called the MTT assay. The MTT assay is a colorimetric method for measuring the activity of mitochondrial enzymes. The enzymes reduce the yellow MTT dye to its insoluble formazan, which has a purple color. Therefore, the amount of formazan formed is proportional to the number of living cells. To determine the cell survival, the 540 nm absorption band is measured in each assay, obtaining an optical density (OD) value at 540 nm wavelength. Microscopic observations and photography were performed using an Olympus BX61 epifluorescence microscope, equipped with an Olympus DP50 digital camera Micromax; Princeton Instruments.

Results & discussion

1. Development of $ZnAl_2O_4$:Nd,Ce nanofibers combining an attractive impregnation sol–gel process and a γ-alumina seed as a support

Fig. 1a presents the measured X-ray diffraction (XRD) data and its modelling using the Rietveld refinement for the $ZnAl_2O_4$: xNd,yCe (x = 0.02, and y = 0.02, 0.04 and 0.06 mol%) doped only

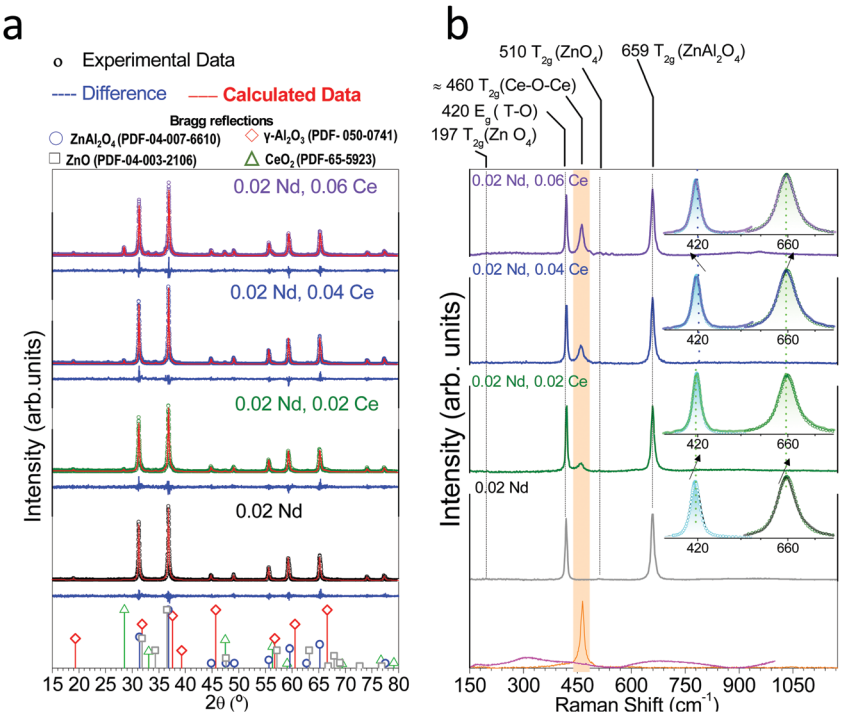

Fig. 1 (a) XRD analysis of the $ZnAl_2O_4$ nanofibers doped with 0.02Nd and co-doped with 0.02Nd 0.02Ce, 0.02Nd 0.04Ce and 0.02Nd 0.06 (mol%). Red, green, gray, and blue peaks at the bottom of the figure represent the reflection positions of γ-Al_2O_3, cerium oxide, zinc oxide, and zinc aluminate phases, respectively. The red line is the fitting obtained, the blue line is the difference and the scatter-line corresponding to each dopant concentration is the experimental data. (b) Raman spectra obtained using 532 nm laser as the excitation source. In the bottom, the Raman spectra of CeO_2 (orange-solid line) and γ-Al_2O_3 (pink-solid line) were included as the reference spectra.

with Nd and co-doped with different Ce doping concentrations annealed at 1200 °C for 2 hours in air.

Well-defined features appear in the XRD patterns obtained from the samples annealed at a temperature of 1200 °C, due to the crystallization of zinc aluminate. In particular, two main peaks appear at 36.8 and 31.2° 2θ, which are associated with (311) and (220) crystallographic planes, marked reflections are in the bottom with a blue square symbol "□" in Fig. 1a, which are characteristics of the facet diffraction of the FCC $ZnAl_2O_4$ phase. The diffraction data are in good agreement with the Joint Committee on Powder Diffraction Standards (Powder Diffraction File (PDF)) card of [PDF: 04-007-6610]. The diffraction peaks confirm that in our system, the annealing temperature above 1200 °C is suitable to obtain polycrystalline $ZnAl_2O_4$ nanofibers. The presence of a "bump" to the high 2θ side of the peaks at 37.8, 44.81, and 65.2° 2θ suggests that the γ-Al_2O_3 phase remains in the structure. Two additional peaks at 28.45 and 47.38° 2θ, corresponding to the crystallographic planes (111) and (220) of Ce, are detected; the marked reflections are at the bottom of Fig. 1a with a green triangle symbol "△".

To further understand the phase composition and site occupation of Zn^{2+} and Al^{3+} cations, Rietveld refinement was performed for $ZnAl_2O_4$:xNd,yCe (x = 0.02 and y = 0.02, 0.04 and 0.06 mol%), as shown in Fig. 1a. All the refinements demonstrated the acceptable R_{wp} factors (Table 1). $ZnAl_2O_4$ has a cubic crystal structure belonging to the spinel compounds having the general formula AB_2O_4, with a space group, O_h^7-*Fd*3*m*, #227; the structure consists of close-packed arrays of oxygen atoms which form 64 tetrahedral sites and 32 octahedral sites. One-eighth of the tetrahedral and one-half of the octahedral sites were occupied by the heterovalent cations. Normal spinels are characterized by the location of the Zn^{2+} cations in tetrahedral sites and Al^{3+} cations in octahedral sites. If Zn^{2+} cations are located in the octahedral sites and, as a consequence, Al^{3+} cations occupy the tetrahedral sites, there is an inversion. Therefore, a whole range of distribution of cations is possible in the spinel-type phosphor which can be represented by the general formula $(M^{2+}{}_{1-\delta}Al^{3+}{}_{\delta})$ $[M^{2+}{}_{\delta}Al^{3+}{}_{2-\delta}]O_4$, where cations inside the round and square brackets are said to occupy the tetrahedral and octahedral sites, respectively. Delta (δ) represents the degree of inversion (defined as the fraction of the tetrahedral site occupied by Al^{3+} cations). If $\delta = 0$, the spinel-type phosphor is normal; when $\delta = 1$, the spinel ferrite is inverse. However, if $0 < \delta < 1$, the spinel is mixed. The degree of inversion has determined some specific physicochemical properties, and their functional behavior can be modulated through the cation distribution. The calculations were done for the *Fd*3*m* space group in which the octahedral 16d sites are shared by Al^{3+} and the tetrahedral crystallographic 8a sites are occupied by Zn^{2+} cations. The refined parameters, lattice parameter, occupancy, oxygen atomic positions, atomic displacement factor for the main phase and the weight percent, are summarized in Table 1 for each sample. Atomic positions and atomic displacement factors did not show discrepancies when compared with values available in the literature. The occupation parameters confirm the presence mainly of Zn^{2+} and Al^{3+} cations in the tetrahedral and octahedral sites, respectively. Around 1–2% of Zn cations occupy the octahedral sites and 2–4% of Al cations occupy the tetrahedral sites. Therefore the degree of inversion is 0.97, 0.97, 0.98 and 0.95 for the $ZnAl_2O_4$ nanofibers doped with 0.02Nd and co-doped with 0.02Nd 0.02Ce, 0.02Nd 0.04Ce and 0.02Nd 0.06 (mol%), respectively. The amount of the different phases after the thermal treatment at 1200 °C is summarized in Table 1. The table indicates the presence of around

Table 1 Rietveld refinement results. *x*,*y*,*z* O-oxygen refined position. Occ Zn tetra-occupation factor of Zn in the tetrahedral site. Occ Al tetra-occupation factor of Al in the tetrahedral site. Occ Zn octa-occupation factor of Zn in the octahedral site. Occ Al octa-occupation factor of Al in the octahedral site. U Zn, Al tetra (Å^2) atomic displacement factor (aka thermal motion parameter) for Zn and Al in the tetrahedral site. U Zn, Al octa (Å^2) Atomic displacement factor (aka thermal motion parameter) for Zn and Al in the octahedral site

	0.02Nd (mol%)	0.02Nd 0.02Ce (mol%)	0.0Nd 0.04Ce (mol%)	0.02Nd 0.06Ce (mol%)
$ZnAl_2O_4$				
Cell param. *a* (Å)	8.0859 (2)	8.0846 (3)	8.0866 (1)	8.0852 (2)
x,*y*,*z* O	0.2648 (2)	0.2646 (2)	0.2652 (1)	0.2651 (2)
Occ Zn tetra	0.971 (4)	0.976 (3)	0.980 (1)	0.951 (2)
Occ Al tetra	0.029 (9)	0.024 (7)	0.020 (1)	0.049 (1)
Occ Zn octa	0.011 (6)	0.018 (2)	0.006 (4)	0.022(2)
Occ Al octa	0.989 (3)	0.982 (3)	0.994 (2)	0.978 (2)
U global (Å^2)	0.0151 (5)	0.0086 (4)	0.0098 (3)	0.0087 (4)
Weight percent (%)	85.5 (8)	79.3 (9)	84.8 (6)	84.2 (6)
Gamma-Al_2O_3				
Cell param. *a* (Å)	5.675 (5)	5.666 (3)	5.662 (2)	5.673 (3)
Cell param. *c* (Å)	7.884 (7)	7.899 (6)	7.890 (4)	7.904 (5)
Weight percent (%)	14.2 (8)	19.7 (8)	14.1 (6)	13.3 (7)
ZnO				
Cell param. *a* (Å)	3.254 (8)	3.246 (7)	3.248 (5)	3.249 (1)
Cell param. *c* (Å)	5.227 (9)	5.199 (6)	5.198 (1)	5.197 (1)
Weight percent (%)	0.3 (1)	0.6 (1)	0.5 (1)	0.8 (1)
CeO_2				
Cell param. *a* (Å)	—	5.420 (9)	5.425 (1)	5.426 (5)
Weight percent (%)	—	0.4 (1)	0.6 (1)	1.7 (1)
R_{wp} (%)	19.22	17.27	12.57	13.52

14% of Al_2O_3; the contribution of secondary phases, such as cerium oxide and ZnO, is quite low, being less than 0.8% for ZnO and 1.7% for cerium oxide. The XRD results allows the determination of the reminiscence of unreacted Al_2O_3 in the presence of $ZnAl_2O_4$ phase.

The average Raman spectra for the Nd doped and Ce co-doped nanofibers are shown in Fig. 1b. The Raman spectra are represented in the Raman shift range of 100–1100 cm^{-1} in Fig. 1b. The irreducible representation for $ZnAl_2O_4$ is Γ: $A_{1g} + E_g + 3T2_{2g} + 2A_{2u} + 2E_u + 5T_{1u} + 2T_{2u}$.[36–39] The Group theory predicts 5 Raman active modes, A_{1g}, E_g, and $3T2_{2g}$. The Raman spectra of the $ZnAl_2O_4$:*x*Nd,*y*Ce, are governed by two main Raman peaks observed around 418–420 and 659 cm^{-1} as well as two small bumps at 197 and 510 cm^{-1}. The Raman peak around 800 cm^{-1} attributed to A_{1g} is not observable. The Raman spectra did not reveal characteristic vibrations of pure ZnO phase that has characteristic Raman modes located at 99, 333, and 438 cm^{-1}.[40] Also, γ-Al_2O_3 is not observed due to the difficulty to detect Raman modes of this phase because the spectrum is usually dominated by the fluorescence background that covers the Raman spectra of γ-Al_2O_3.[41] The samples co-doped with cerium exhibit also a Raman mode corresponding to the Ce–O–Ce symmetrical stretching vibration of the oxygen atoms around cerium cations[42,43] The Raman peak at 545 cm^{-1} can be ascribed to the oxygen vacancies introduced into the ceria lattice to maintain charge neutrality when Ce^{4+} cations are re placed with trivalent cations.[44]

The $T_{2g}(1)$ (197 cm^{-1}) mode is assigned to a complete translation of the AO_4 tetahedra within the spinel structure and $T_{2g}(2)$ is assigned to the motion of cations occupying only the tetrahedron. These modes in the samples are quite weak, and only small bumps located in these Raman shifts are recognizable. The main Raman peak around 418–420 cm^{-1} is assigned to the E_{1g} asymmetric bending motion of the oxygen atoms within the tetrahedral sites. The Raman mode $T_{2g}(3)$ at 659 cm^{-1} is related to the nature of the octahedral cation, following the analogy of $ZnGa_2O_4$ structure characterization.[45] It has been stated that the E_g peak position is affected by the type of cation occupying the tetrahedrally and octahedrally coordinated sites and the E_g peak shifts to lower wavelengths when the cation radius is higher. In case the Nd occupies the tetrahedral sites, its cation radius is higher (Nd: 0.983 Å), in comparison with the Zn radius (Zn: 0.569 Å). In comparison with the undoped sample, the incorporation of 0.02Nd mol% leads to a Raman shift of the peak from 419.97 (undoped sample) to 418.48 cm^{-1}. The FWMH also changes from 5.9 to 6.4 cm^{-1} due to the effect of the occupational disorder. This behavior is also observable for the Raman peak around 659 cm^{-1}; the position changes from 659.16 to 658.89 cm^{-1}. The peak is slightly broader (9.57 to 10.45 cm^{-1}). It means that the addition of Nd causes cation disorder and as a consequence all the Raman peaks broaden.[46] It seems that the incorporation of cerium does not have an evident disorder in the structure. The E_g peak as well as the $T_{2g}(3)$ peak shift to higher wavelengths and the FHWM is higher than the FHWM of the undoped sample but not higher than that of the sample doped only with Nd.

An impregnation process through the sol–gel route followed by annealing was selected to make use of the γ-Al_2O_3 nanofiber morphology used as the precursor. The as-received γ-Al_2O_3 fibers are of 200 nm to 1.2 μm long with a smooth surface of 20–50 nm diameter and were used as the precursors. The characterization of γ-Al_2O_3 is summarized in SI.1. (see ESI,† Fig. S1). By the synthesis strategy proposed, the morphology of the as-received nanofibers is retained to synthesize the $ZnAl_2O_4$:Nd,Ce nanofibers. The γ-Al_2O_3 precursor was used as a template to control the $ZnAl_2O_4$ growth. The morphology and diameter of the synthesized nanofibers were examined by field emission scanning electron microscopy (FE-SEM) and high-resolution transmission electron microscopy (HR-TEM). After annealing at 1200 °C for 2 h, the synthesized compounds retain the morphology of nanofibers, but the length decreases due to the sonication that breaks the fibers into shorter strands (Fig. 2a). As shown in the low magnification TEM image in Fig. 2b, the average diameter of nanofibers is 50 nm. Crystal planes of a $ZnAl_2O_4$ domain can be observed, Fig. 2c. Large scale crystal lattice fringes can be obviously seen, which indicate the excellent crystallization of the $ZnAl_2O_4$ grains. Distance *d* spaces of ~2.08 and 4.6 Å correspond to the (022) and (111) crystal planes of the $ZnAl_2O_4$ phase, respectively. The fast Fourier-transformed pattern in the inset of Fig. 2c shows the ⟨110⟩ growth direction, as shown in the schematic of Fig. 2d.

A detailed interpretation of the kinetics of the reaction and formation of $ZnAl_2O_4$ crystals was also carried out, as shown in the scheme in Fig. 2d. The first stage in the formation of $ZnAl_2O_4$ crystals from the impregnation of the gamma-alumina fibers (stage I in the scheme in Fig. 2d) is the oriented nucleation along the pre-existent γ-Al_2O_3 fibers. The nanofibers can appear aggregated, forming bundles or without aggregation (stage II in the scheme in Fig. 2d). The nanofibers are aggregated more or less parallel, forming small angles in bundles. The nucleation continues and the crystals start to grow around the nuclei; the segmented fibre structure appears to be retained during the growth of crystals. These segmented entities of rectangular shape, which are designated as laths, are the fragments of the block which form the entire fiber (stage III in the scheme in Fig. 2d). These crystalline laths or domains are orderly arranged along the axial direction of the single nanofiber. The schematic shows ⟨110⟩ closed-packed chains, which are formed during crystallization. This ⟨110⟩ growth can occur without a seed, and that is how the first $ZnAl_2O_4$ crystallite is formed, which acts as a template for the successive formation of $ZnAl_2O_4$ nanolaths (prismatic crystals elongated along the ⟨110⟩ direction). Nanolaths aggregate and form rods from the units designated such as the laths. The width of the rods is in the nanometric scale of ~50 nm, and this dimension is limited by the initial diameter of γ-Al_2O_3 fibers. The length of the fibers can vary greatly as we explained before due to the sonication process that breaks the fibers into shorter strands.

From the previous microstructural and morphological characterization the presence of unreacted γ-Al_2O_3 fibers is not evident. However, the presence of remaining γ-Al_2O_3 as the secondary phase was revealed through the XRD analysis. The formation of the spinel $ZnAl_2O_4$ solid solution is governed by a solid-state diffusion mechanism. In our case, the use of γ-Al_2O_3

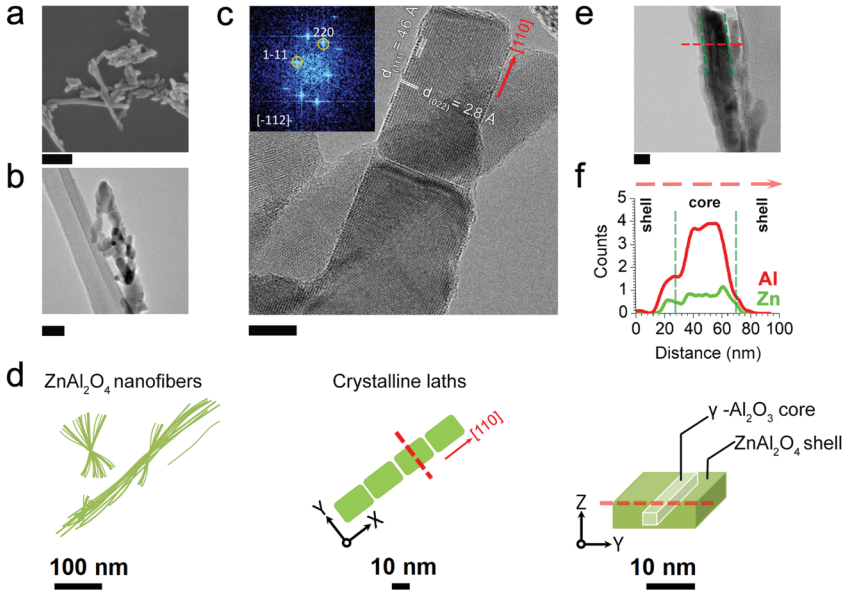

Fig. 2 Microstructural and morphological characterization of the $ZnAl_2O_4$ nanofibers synthesized: (a) FE-SEM micrographs of the $ZnAl_2O_4$ nanofibers (scale bar corresponds to 100 nm). (b, c and f) HRTEM image of the $ZnAl_2O_4$ nanofibers (scale bar in b and c corresponds to 50 and 10 nm, respectively). (d) Scheme of the kinetics of the reaction and formation of $ZnAl_2O_4$ (e) EDS line-scan analysis of co-doped 0.02Nd 0.02Ce (mol%) $ZnAl_2O_4$ nanofibers.

as a seed fiber alongside the impregnation method could imply the formation of a spinel phase layer such as the external cover of the γ-Al_2O_3 nanofiber because the surface diffusion processes are favored over the volume diffusion processes. As a consequence, the complete reaction between ZnO and Al_2O_3 is limited by the kinetic reaction. The diffusion of Zn *via* the $ZnAl_2O_4$ interface controls the rate formation at a higher temperature of 1200 °C. Assuming that the $ZnAl_2O_4$ restricts the complete formation of the spinel phase, it is expected that some γ-Al_2O_3 remains in the core of the $ZnAl_2O_4$ nanofibers. For this reason an energy dispersive spectrum (EDS) line scan was carried out in the $ZnAl_2O_4$ nanofibers to evaluate this possible proposed scenario in the impregnation process.

Fig. 2e shows the TEM micrograph of the $ZnAl_2O_4$ nanofibers co-doped with 0.02Nd 0.02Ce (mol%) and Fig. 2f presents the EDS line profile showing the distribution of Zn, Al along the fibre. The EDS profile also displays direct evidence of the formation of the core–shell structure (Stage IV in the scheme in Fig. 2d). The Al related counts show the maximum at the core region and the Al is also present at the shell zone due to the contribution of the $ZnAl_2O_4$ phase as a 3–5 nm layer (marked in the figure) and Zn is present along all the profile. It is important to mention that due to the small amount of Nd and Ce present in the fibers, EDS cannot detect them because it is out of the range of measurement of the technique. However, the presence of both elements is confirmed by XANES, XPS and optical spectroscopy as described in the next sections. The line-scanning analysis agrees with the XRD results.

2. Luminescence properties of $ZnAl_2O_4$:Nd,Ce nanofibers

Fig. 3a–e show the luminescence response of the $ZnAl_2O_4$ nanofibers doped with neodymium and co-doped with cerium. The excitation spectra of the 1059 nm emission ($^4F_{3/2} \rightarrow {}^4I_{11/2}$) are shown in Fig. 3a. The excitation spectra show that 359 nm is the strongest excitation wavelength for 1059 nm emission for the material co-doped with cerium. Besides, the excitation wavelengths assigned to Nd are also observable. From the NIR emission spectra, it can be seen that there are three emission regions from 860 to 970 nm ($^4F_{3/2} \rightarrow {}^4I_{9/2}$); 1020 to 1200 nm ($^4F_{3/2} \rightarrow {}^4I_{11/2}$) and 1280 to 1400 nm ($^4F_{3/2} \rightarrow {}^4I_{13/2}$). The emission around 1059 nm consists of three peaks, which are at the wavelength of 1047, 1059, and 1079 nm. All of the emission peaks are assigned to Nd emitters. The peak intensity of Nd^{3+} emission at 1059 nm under λ_{EXC} = 359 nm is greatly enhanced by the co-doping of Ce. This indicates that there is Ce → Nd energy transfer in the down-conversion luminescence process. The $ZnAl_2O_4$ nanofibers doped only with Nd do not show emission peaks under excitation at 359 nm (see the detailed spectrum of Fig. 3a in Fig. 3e), this corroborates that co-doping enhances the emission in the NIR range. The UV-vis absorbance spectra shown in Fig. 3c confirm the Ce absorption; the broad band located in the 250–400 nm range assigned to Ce absorption is observable in $ZnAl_2O_4$ nanofibers co-doped with Nd–Ce. From the absorption spectrum acquired in the 200–900 nm range of the $ZnAl_2O_4$ undoped nanofibers, the small absorption band below 374 nm assigned to the host is visible. With the incorporation of cerium, a broad absorption band appears; starting to appear at 397 nm. This band is related to cerium absorption. For the Nd and Ce co-doped samples the broad band of cerium is present as well as different absorption peaks related to neodymium.

The nanofibers can be also excited directly by different excitation peaks that are located at 514, 527, 583, 685, 742, 801 and 825 nm assigned to $^4G_{9/2}$; $^4G_{7/2}$; $^4G_{5/2}$, $^4G_{7/2}$; $^4F_{9/2}$; $^4F_{9/2}$, $^4S_{3/2}$; and $^4F_{5/2}$, $^4H_{9/2}$ excited state of Nd^{3+} cations, respectively, that are present in both excitation (Fig. 3a) and absorption spectra (Fig. 3c). When the amount of cerium increases the band related

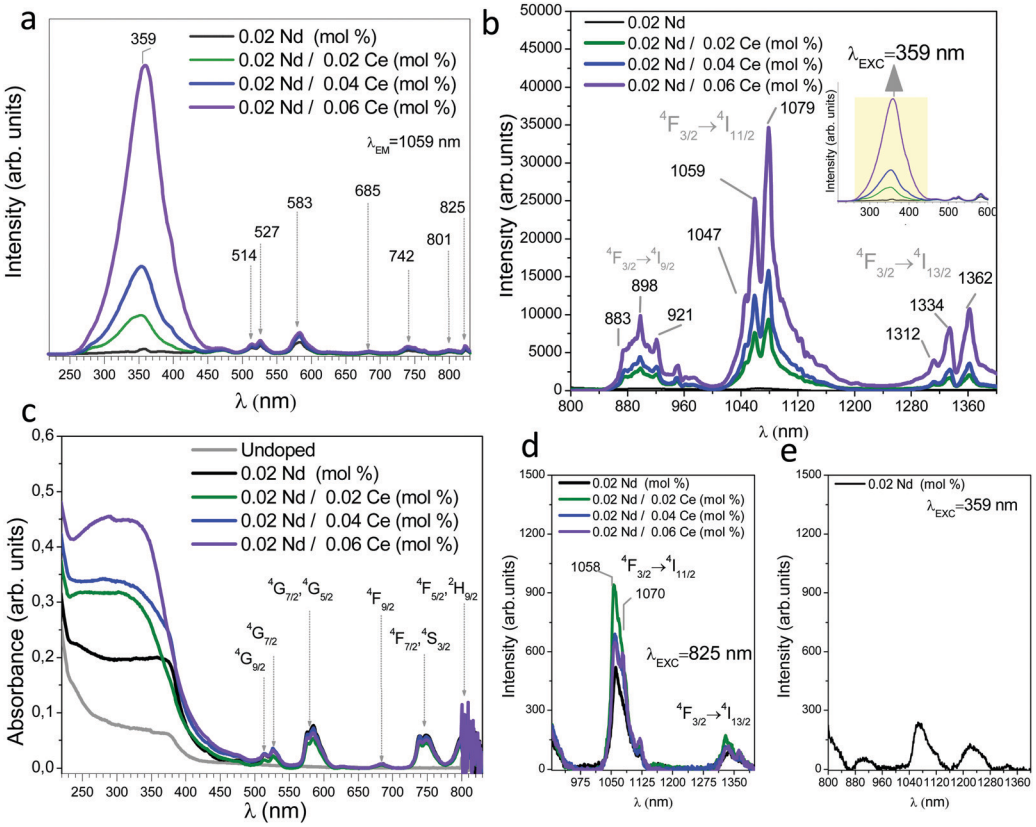

Fig. 3 Optical spectroscopy study corresponding to the $ZnAl_2O_4$ nanofibers undoped, doped with 0.02Nd and co-doped with 0.02Nd 0.02Ce, 0.02Nd 0.04Ce and 0.02Nd 0.06 (mol%): (a) excitation spectrum recorded at emission wavelength 1059 nm. (b) Emission spectra under 359 nm excitation. The inset shows that the stronger excitation band is located at 359 nm. (c) UV-VIS-NIR absorption spectra. (d) Emission spectra under 825 nm excitation. (e) Detailed emission spectrum of the sample doped only with Nd under 359 nm.

to Ce absorption increases as well. Under 825 nm (Fig. 3a), the strongest emission band covering 1020–1139 nm is assigned to the transition $^4F_{3/2} \rightarrow {}^4I_{11/2}$, and the other band covering 1239–1400 nm is ascribed to the $^4F_{3/2} \rightarrow {}^4I_{13/2}$ transition. With the incorporation of Ce, the emission band is almost similar for all concentrations, indicating that only Nd is important under 825 excitation (Fig. 3d). It is important to remark that fluorescence imaging is a useful technique for bio-imaging and bio-sensing applications. Specifically for *in vivo* bio-medical applications, it is better to use the NIR region due to the low absorption and autofluorescence from the tissues, improving the penetration depth. It is advisable that the excitation and emission wavelengths should be confined within the biological transparency window (700–1000 nm). Therefore, as it can be inferred from Fig. 3d, both emission and excitation wavelengths of $ZnAl_2O_4$ nanofibers co-doped with Nd–Ce are located in the optical window of cells and tissues (700–1100 nm). However, the UV-visible excitation can serve complementarily due to the superficial sensing depth, for use in pre-clinical tumor assays, as well as, in *in vivo* if the excitation of the biomarker in the visible range is relatively harmless to the body of animals.[47,48]

Based on our observations, where the emission intensity for the NIR emission strongly increases with the cerium incorporation in comparison with the sample doped only with Nd (Fig. 3e), the emission could be related to the charge energy transfer from Ce to Nd^{3+}. It is not possible to state if the energy transfer and the enhancement are due to Ce^{3+} or Ce^{4+} cations. As we explained in the Introduction section, the absorption bands of cerium in the trivalent state are 2 times narrower than the electron-transfer bands of cerium in its tetravalent state. Therefore, it is expected that the enhancement would be related to cerium in its tetravalent state. However, from photoluminescence experiments it is difficult to generate a clear statement. We can conclude that when the $ZnAl_2O_4$ nanofibers co-doped with Nd–Ce are excited directly at 825 nm, an emission peak centered at 1058 nm related to Nd transition appears, indicating the potential of these compounds to be suitable candidates for biological markers. In addition, it is possible to make use of the excitation out of the biological transparency window (700–1000 nm) for *in vitro* and specific bio-imaging studies, which use superficial sensing depth for analysis in the pre-clinical assays rather than the sub-surface assays.

The main result obtained for the first time to our knowledge is that we can significantly increase the emission in the NIR range with the incorporation of a low amount of cerium cations. Three main emission bands related to Nd^{3+} cations have been observed for these samples centered at 898 nm, 1079 nm, and 1362, while the most intense peak is at 1087 nm, which is the most interesting from the application point of view. $ZnAl_2O_4$ nanofibers co-doped with Nd–Ce are good

candidates as phosphors for *in vitro* bioimaging purposes with the intense emission produced through energy transfer from Ce to Nd after excitation in the UV spectral region.

3. Understanding $ZnAl_2O_4$:Nd,Ce nanofiber structure–property relationship

The local structure surrounding the Zn^{2+}, Ce^{3+}, Ce^{4+} and Nd^{3+} cations was explicitly studied across the $ZnAl_2O_4$ nanofibers undoped, doped with Nd and co-doped with different concentrations of cerium (0.02, 0.04 and 0.06 mol%), by using the XAS to investigate the X-ray absorption near edge structure (XANES) and the extended X-ray absorption fine structure (EXAFS) to determine the local structure. The XANES spectra were collected at the Ce L_3-edge and Nd L_2-edge for the doped $ZnAl_2O_4$:*x*Nd,*y*Ce (*x* = 0.02 and *y* = 0.02, 0.04 and 0.06 mol%) nanofibers and are shown in Fig. 4a–e.

The Ce L_3-edge exhibits the presence of mixed-valence cerium, which makes the XAS complex (Fig. 4a). The XANES spectra for all the $ZnAl_2O_4$:*x*Nd,*y*Ce (*x* = 0.02 and *y* = 0.02, 0.04 and 0.06 mol%) nanofibers show two well-resolved white lines similar to the spectra of mixed-valence Ce. The characteristic white line at 5727.66 eV of a typical Ce^{3+} is observed in *e.g.*, $Ce(NO_3)_3{\cdot}6H_2O$ compound. The spectrum of CeO_2 exhibits a double white line characteristic of the two cerium ground-state electronic configurations, $4f^0$ and $4f^1$. The main peak located at 5731.92 is assigned to the final state of $2p4f^15d^1v$ and attributed to Ce^{4+}. Additionally, the spectra show another peak at an energy of 5738.97 eV, nearly 7 eV above the main white line which can be ascribed again to the Ce^{4+} electronic configuration (the final state of $2p4f^05d^1v$).

Different approaches have been proposed to support the analysis of Ce XANES spectra. The four peak fitting where a pre-edge feature (Peak a) located at 5715 eV due to dipole-forbidden $2p_{3/2} \rightarrow 4f$ transition, two main features located at 5735 (Peak c) and 5726 eV (Peak d) due to the mixture of the multi-electron configurations $L4f^05d^1$ and $L4f^15d^1$ and a low energy peak located at 5722.5 eV (Peak b) due to the splitting of Ce 5d states in the cubic crystal field of the oxygen is considered.[49,50] The observed peaks in the Ce L_3-edge XANES spectra were fitted with Gaussian or Lorentzian functions and arctan functions were added to simulate the continuum edge jump in the spectra.[51] Another approximation was done by Overbury *et al.* estimating the height difference between peak b and peak d, after subtracting a standard Ce^{3+} spectrum.[52] Other authors employed linear combination fitting (LCF), assuming that the XANES spectrum of the samples at the Ce L_3 edge is composed of a weighted sum of a standard Ce^{4+} (micron-sized CeO_2) spectrum and a standard Ce^{3+} (micron-sized Ce_2S_3) one. In this case, the fraction of each phase (Ce^{3+} and Ce^{4+}) is given by the weight factor of the spectra. It is important to remark that this approach assuming that CeO_2 as a standard for 100% Ce^{4+} and 0% Ce^{3+}[53] is not totally true because CeO_2 contains traces of Ce^{3+}.[49]

The ratio of the fractions of Ce^{4+} and Ce^{3+} ions was determined by using LCF to obtain the Ce^{3+}/Ce^{4+} concentrations in $ZnAl_2O_4$:0.02Nd,*y*Ce (*y*: 0.02, 0.04 and 0.06) co-doped nanofibers and by assuming that the Ce L_3-edge XANES spectra of $ZnAl_2O_4$:0.02Nd,*y*Ce co-doped nanofibers are a linear combination (LC) of a CeO_2 spectrum and a $Ce(NO_3)_3{\cdot}6H_2O$ spectrum. As we stated previously, CeO_2 contains traces of Ce^{3+}, the *x*-axis represents the relative increment of Ce^{4+}, considering the Ce^{3+} trace in CeO_2 as a constant in all the samples. It should be emphasized that the percentage of photoluminescence intensity increases accordingly with the quantity of cerium incorporated in the $ZnAl_2O_4$ structure. A higher concentration of the sensitizer, Ce, implies a higher concentration of the Ce^{4+} fraction, as seen in Fig. 4b (see ESI,† Fig. S2). The coexistence of Ce^{3+} and Ce^{4+} and the ability to control their relative fraction allow the design and preparation of new NIR emitting materials.

Concerning the EXAFS studies in Ce L_3-edge, the distance Ce–O in Ce_2O_3 is approx., 2.1 Å, while in in CeO_2 is approx., 2.2 Å. In this study, the Ce–O distance is found to be around 2.3 Å and it progressively decreases from $R = 2.34 \pm 0.01$, 2.32 ± 0.01 and

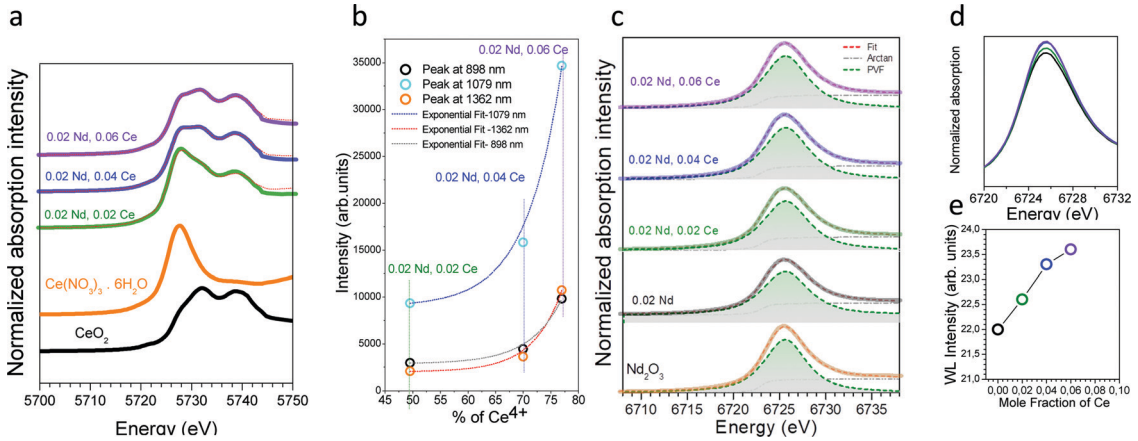

Fig. 4 XANES analysis of the Ce L_3-edge and Nd L_2-edge to the $ZnAl_2O_4$ nanofibers co-doped with 0.02Nd and 0.02, 0.04 or 0.06Ce (mol%). (a) XANES spectrum of the samples at the Ce L_3 edge. The fitting of each sample is presented with the dashed red-line. (b) Luminescence intensity centered at 898, 1079, and 1362 nm as a function of the percentage of Ce^{4+} calculated for each sample. (c) XANES analysis of the Nd L_2-edge, showing the linear combination fitting (LCF) for XANES of Nd L_2-edge white line using an arctan (dashed pink) with a pseudo-Voigt function (PVF, dashed blue). (d) White line intensity detailed study of Nd L_2-edge. (e) WL intensity as a function of the Ce doping level.

2.31 ± 0.01 Å for samples doped with 0.02Nd and co-doped with 0.02, 0.04 and 0.06Ce (mol%), when the Ce content increases. Regarding the σ^2 (DW factor), the general tendency is to decrease with an increase in the Ce content. For the lowest doped level, a higher disorder is observed ($20 \pm 10 \times 10^{-3}$ Å^2) as compared to the highest doped level ($5 \pm 1 \times 10^{-3}$ Å^2). This fact could be associated with the formation of clusters for higher doping levels.

The XANES spectra of Nd_2O_3 reference at L_2-edge together with the Nd-doped and Nd–Ce co-doped nanofibers are shown in Fig. 4c. The Nd_2O_3 standard exhibits the L_2-edge XANES spectrum with a sharp white line at 6723 eV and two small features at 6737 and 6758 eV. The XANES spectra were fitted by an arctan plus a pseudo-Voigt function. The error bar for the WL intensity is ~0.004, hence it is inside the spot size, and it was estimated by the the maximum difference between the intensity of the spectra. Very good fits are obtained as indicated by the low *R*-factor. XANES analysis shows that the absorption edge position does not change with the increase of Ce concentration. A detailed inspection of the WL intensity shows that the WL intensity increases with Ce-doping (Fig. 4d). To interpret the intensity of RE L_2 and L_3-edges, in our case the Nd L_2-edge, the intensity is determined by the density of unoccupied 5d states and the transition matrix elements. Usually, the stronger WL intensities can be assigned to the degree of covalent bonding between the rare earth and ligands. The variation of WL intensity is ascribed also to the competition between oxygen vacancies and localization of RE-d states.[54,55] Generally, the WL intensity decreases at higher doping concentrations due to the higher quantity of oxygen vacancies.[54,55] Here, the Nd L_2-edge WL intensity shows an increase with Ce-doping (Fig. 4e), suggesting an increase of the localization of the RE empty *d* density of states.

In principle, the study of the Zn K edge may provide information about the oxidation state and, in some cases, allows the separation of the contributions of the Zn cations in tetrahedral and octahedral sites. With insights derived from inspecting the XANES spectra, the analysis confirms the EXAFS results. The Zn K edge XAS spectra of references such as $Zn(NO_2)_3{\cdot}6H_2O$ and ZnO together with $ZnAl_2O_4$ undoped and 0.02Nd, 0.06 (mol%) Ce co-doped nanofibers are shown in Fig. S2a and b (ESI†). From XANES results of the Zn K edge, there is no considerable difference between the undoped and the highest doped samples, so we cannot conclude a rough indication of tetrahedral or octahedral units. However, the presence of the four features at 9663, 9667 and 9672 eV and a shoulder at 9678 eV can be assigned mainly to tetrahedral contribution. From EXAFS experimental results obtained, in particular the Fourier transform (FT) at the Zn K-edge, a low degree of inversion seem to be present since at the Zn K-edge the most intense peak is centered at about 3 Å (mostly tetrahedral environment) (see ESI,† Fig. S2b). These results corroborate the results obtained from XRD refinements.

To study the electronic structure of the Nd-doped $ZnAl_2O_4$ and Ce co-doped nanofibers, the high-resolution photoelectron spectra of Zn, O, Al and Ce core levels were recorded and are shown in Fig. 5a–c and 6, respectively. The analysis of the XPS yields the detailed chemical composition at the nanofiber surface. To determine the positions of the various components, the spectra were deconvoluted using a peak fitting process. The Zn 2p core-level spectra of nanofibers recorded at RT exhibit a doublet assigned to Zn $2p_{3/2}$ and Zn $2p_{1/2}$ located around 1022 and 1045 eV (Fig. 5a). Druska *et al.*[56] established that tetrahedrally coordinated species exhibit a peak related to Zn $2p_{3/2}$ around the 1020–1022 eV range for ZnO and $Zn_2Ti_3O_8$ compounds. The $ZnAl_2O_4$ undoped nanofibers show a single sharp peak that corresponds to the tetrahedrally coordinated Zn located at 1022.1 and 1045.3 eV. A second component starts to appear at energies, around 1023–1024 eV being assigned to the octahedrally coordinated Zn that is in an agreement with octahedral compounds such as Zn_2TiO_4 and $ZnTiO_3$. The undoped, Nd-doped and Nd–Co co-doped with 0.02 and 0.04Ce (mol%) samples show a second component for the Zn $2p_{3/2}$ line at 1023.4 and 1025.6 eV, and for Zn $2p_{1/2}$ line at 1045.1 and 1045.6 eV, respectively. The appearance of a second peak at higher binding energies suggests the presence of octahedral Zn^{2+} cations. After doping of neodymium in the material, both the spectra of the Zn $2p_{3/2}$ and Zn $2p_{1/2}$ core levels show a 0.1 eV and 0.2 eV shift toward lower binding

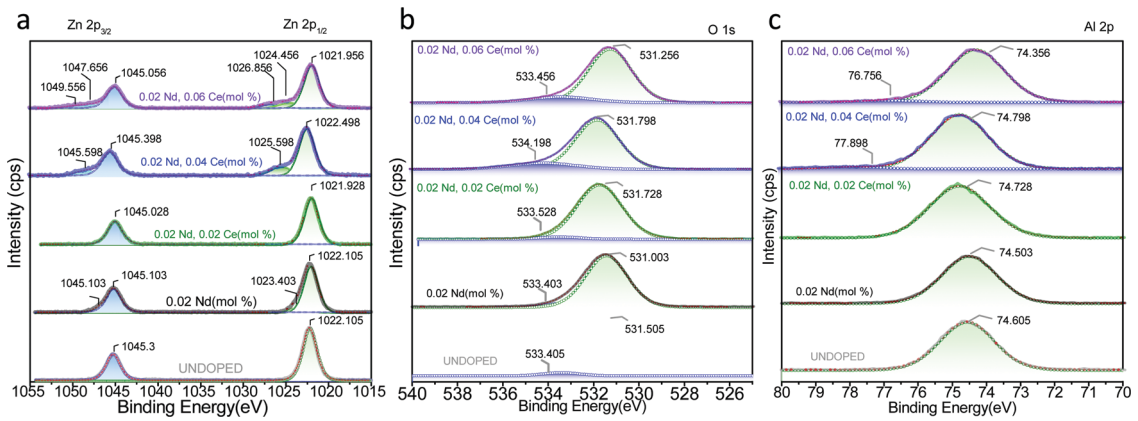

Fig. 5 XPS analysis of $ZnAl_2O_4$ nanofibers undoped, doped with 0.02Nd and co-doped with 0.02Nd 0.02Ce, 0.02Nd 0.04Ce and 0.02Nd 0.06 (mol%): the experimental solid line and fitted curves (dot curves for each peak and solid red line for the sum of the deconvolution) of high-resolution XPS spectra of (a) Zn $2p_{3/2}$ and Zn $2p_{1/2}$ 2 (b) O 1s. (c) Al 2p lines.

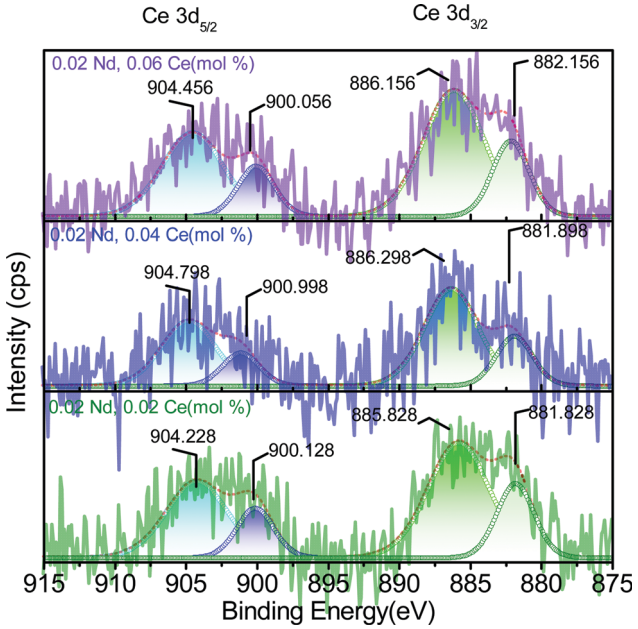

Fig. 6 XPS analysis of $ZnAl_2O_4$ nanofibers co-doped with 0.02Nd 0.02Ce, 0.02Nd 0.04Ce and 0.02Nd 0.06 (mol%): the experimental solid lines and fitted curves (dot curves for each peak and solid red line for the sum of the deconvolution) of high-resolution XPS spectra of Ce $3d_{3/2,5/2}$ lines.

energies when the concentration of Nd^{3+} goes to 0.02 (mol%). These changes can be a consequence of modification in Zn–O bonding upon Nd doping. The electronegativity of Nd^{3+} is smaller that of Zn^{2+} and thus results in a decrease in the binding energy of Zn 2p electrons.

The co-doping with 0.02Nd and 0.02Ce (mol%) leads to a shift of the two peaks to lower binding energies in comparison with the undoped sample, but did not show the appearance of second peaks. Therefore, it can be assumed that Nd–Ce co-doping with Ce in a low concentration (0.02 mol%) produces a balancing process that does not distort the structure towards an inverse spinel or a low degree of inversion observable by XPS.

However, high concentrations of Ce-doping (0.04 and 0.06 mol%) reveal the appearance of the second and third peaks. The second peaks are related to octahedrally coordinated Zn. These results corroborate the findings observed by the XRD refinements.

Fig. 5b shows the XPS peak of O 1s. The O 1s line consists of two peaks located around 531.0–531.7 and 533–534 eV. The peak at 531.7 eV is assigned to the O sites of the spinel lattice, probably the peak is related to AlO_x (Al in the AlO_4 tetrahedral site or the AlO_6 octahedral site). The XPS peak located at 532 eV is ascribed to the chemisorbed O or hydroxyl species.[57,58] Both XPS peaks exhibit a shift to higher energies for the Nd–Co co-doped samples in comparison with the undoped one. Again, the sample doped only with Nd demonstrates a different behavior, and the peaks have a shift to low energies.

The Al 2p signal is relatively broad, the Al 2p spectra are more asymmetric with the incorporation of dopants (Fig. 5c). This indicates that the Al^{3+} ions occupy more than one coordination environment. The main peak is located in the range of 74.3–74.8 eV. The direction of the chemical shift is towards low energies. The incorporation of 0.04Ce (mol%) leads to the appearance of a second peak at 77 eV. The FWHM of the peak increases with the incorporation of Ce. The peak at the lower binding energy can be ascribed to the Al^{3+} ions at the tetrahedral sites, whereas the peak at higher binding energy can be assigned to the Al^{3+} ions that occupy the octahedral sites.[59]

The main feature of the surface elemental structural disorder of the undoped, Nd-doped, and Nd–Ce co-doped samples is that co-dopants induced the spinel inversion and the inversion degree increases with an increase in the Ce content.

The Ce $3d_{3/2,5/2}$ spectra are composed of two multiplets corresponding to the spin–orbit split $3d_{5/2}$ and $3d_{3/2}$ core electrons, and two features are present in each spin–orbit component. These four peaks can be attributed to Ce (Ce^{3+} cations). The satellite peak associated with the Ce $3d_{3/2}$, characteristic of the presence of tetravalent Ce (Ce^{4+} cations) in Ce compounds, located at 916.9 eV is not observable in the samples. The peaks located at 904 and 886 eV are the results of the Ce $3d^94f^1$ O $2p^6$ final state and the peaks at 900 and 882 eV are the result of Ce $3d^94f^2$ O $2p^5$.[60] It can be observed from XPS results that the nanofibers present mainly Ce^{3+} in comparison with the results presented by XANES. It is necessary to take into account that XPS is a surface characterization technique and usually overestimates the Ce^{3+} content.[61] Also, the XPS determination of the cerium oxidation state in compounds faces difficulties due to the complex structure in the valence- and core-electron spectra.[62]

4. Cytotoxicity-cell viability assays of $ZnAl_2O_4$:Nd,Ce nanofibers

To evaluate the applicability of $ZnAl_2O_4$ nanofibers as biomarkers, the cytotoxicity of nanofibers was tested. The cytotoxicity assay is performed on tumor epithelial cell line HeLa (Fig. 7a and b). The HeLa cells were incubated with 1, 10 and 100 μg mL^{-1} concentrations of $ZnAl_2O_4$ nanofibers for 24 h. After that, the cell viability was determined using 3-(4,5-dimethylthiazol-18 2-yl)-2,5-diphenyltetrazolium bromide, the MTT assay.

The cell survival, as determined from the 540 nm absorption band, is measured in each assay. The MTT assay provides the readout of the optical density at 540 nm as shown in Fig. 7b. The results indicate that the sample has little influence on the viability and proliferation of HeLa cells. The optical density is higher than the control for 1 and 10 μg mL^{-1} concentrations. Even if, the concentration of the sample reaches 100 μg mL^{-1}, the viability of the cells does not present a decreasing trend. A slight increase of the optical density in comparison with the control from 0.16 to 0.19 was observed. The OD value of a non-treated/standard/control population of cells (the theoretical 100%) and the ratio of the treated cells' OD value to the non-treated cells are used for representing the viability in percent (see ESI,† Fig. S3). MTT assays and related assays rely on a mitochondrial reductase to convert the tetrazole to formazan. The assumption is that the conversion is dependent on the number of viable cells but there is always the possibility that treatment of the cells may result with increased enzymatic activity without actually having an effect on the cell number or cell viability. If the OD of treated cells is 10% as example

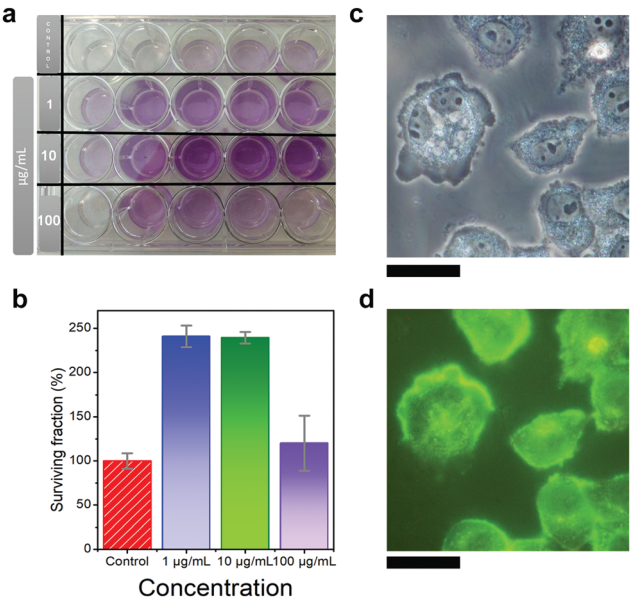

Fig. 7 Evaluation of cytotoxicity. (a) MTT assay – the HeLa cells were incubated with 1, 10 and 100 μg mL^{-1} concentrations of $ZnAl_2O_4$ for 24 h, and a control is also evaluated. (b) Error bars represent mean ± SE, 5 cultures. (c and d) Visualization of HeLa cells in the presence of $ZnAl_2O_4$ nanofibers by wide field fluorescence microscopy After 24 h of incubation, cells were first imaged by (c) phase contrast and then (d) by UV excitation using a UV filter (λ_{exc}: 340–380 nm). Under UV excitation, cell autofluorescence appeared in green while $ZnAl_2O_4$ nanofibers' fluorescence appeared in bright green. Scale bars correspond to 20 μm.

higher than the OD of the control group, it does not necessarily mean that the treated cells are 10% more viable. From the results carried out, it is possible to deduce that the $ZnAl_2O_4$ nanofibers do not exhibit cytotoxicity activity. Previous studies on $ZnAl_2O_4$ established the viability of $ZnAl_2O_4$:Nd^{3+} nanoparticles using bone marrow stromal cells, as well as, the viability and adhesion of the $ZnAl_2O_4$ nanostructured thin films using human osteoblastic cells.[11,63] The visualization of HeLa cells in the presence of $ZnAl_2O_4$ nanofibers by wide field fluorescence microscopy is shown in Fig. 7c and d. After 24 h of incubation, the cells were first imaged as shown in Fig. 7c, phase contrast, and then as shown in Fig. 7d by UV excitation using a UV filter. Preliminary studies indicate the localization of tested $ZnAl_2O_4$ nanofibers around the cells that present a rounded and epithelial aspect. The results show that $ZnAl_2O_4$ nanofibers are promising biomarkers for HeLa-cell tracking.

Conclusions

In this study, we have successfully developed a cost-efficient procedure to prepare $ZnAl_2O_4$:Nd,Ce NIR luminescent nanofibers, which considerably facilitates their large scale production. The synthesis of the uniform-sized nanofibers was performed *via* the method of a facile sol–gel combined with an annealing procedure.

This work provides extensive and direct evidence of the role of Ce^{4+} in the energy transfer to Nd^{3+} in order to enhance the NIR emission that has remained absent in understanding the down-conversion process between cerium compounds. The extension of the developed procedure to other lanthanide-based $ZnAl_2O_4$ nanofibers is the subject of future work. Nd--Ce co-doped $ZnAl_2O_4$ nanofibers have been shown to be excellent NIR phosphors due to the excitation through the Ce–Nd energy transfer band. These materials hold great potential for use for *in vitro* bio-labeling applications. On the other hand, they showed emission in the near-infrared field after excitation at 825 nm, which is interesting for deep tissue fluorescence bioimaging. The viability of the material was demonstrated by the cytotoxicity studies performed.

Author contributions

The samples were prepared by R. E. R.-H. The structural, microstructural and optical characterization of the samples was performed by R. E. R.-H., F. R.-M., I. H., G. G. and J. F. F., F. R.-M. and L. P. participated actively on TEM characterization and analysis. R. E. R.-H. collaborated specifically on photoluminescence characterization and intensely on XANES analysis with G. G. and C. M. The manuscript was written by R. E. R.-H., edited by F. R.-M., L. P., I. H., G. G., C. M., M. D., R. U. I., and J. F. F., and approved by all authors. All authors contributed to discussions and reviewed the manuscript.

Conflicts of interest

The authors declare no competing financial interests.

Acknowledgements

This work was supported by the Spanish Ministry of Science Innovation and Universities (MICIU) under the projects MAT2017-86450-C4-1-R, and the Spanish National Research Council (CSIC) under the project NANOMIND CSIC 201560E068. R. E. R.-H. acknowledges the financial support from the Estonian Research Council (ETAG) through the European Regional Development Fund and the programme Mobilitas Pluss (Grant No. MOBJD254). The support of the ETAG through PSG 466 (R. E. Rojas-Hernandez) is also acknowledged. F. R.-M. is indebted to MINECO for a 'Ramon y Cajal' contract (ref: RyC-2015-18626), which is co-financed by the European Social Fund. F. R.-M. also acknowledges support from a 2018 Leonardo Grant for Researchers and Cultural Creators (BBVA Foundation). The support of the ETAG through PRG643 (I. Hussainova) is also acknowledged. We express thanks to the Maarja Grossberg group for allowing us to use the laboratory facilities. M. Danilson acknowledges the European Union through the European Regional Development Fund, Project TK141. Part of these experiments was performed at the CLAESS beamline at ALBA Synchrotron with the collaboration of ALBA staff. R. E. R.-H. would like to acknowledge Prof. Vitali Nagirnõi and Dr Ivo Romet for their insightful suggestions and all the experiments performed by them to clarify the results.

References

1 N. Pathak, P. S. Ghosh, S. Saxena, D. Dutta, A. K. Yadav, D. Bhattacharyya, S. N. Jha and R. M. Kadam, *Inorg. Chem.*, 2018, **57**, 3963–3982.
2 D. P. Dutta, R. Ghildiyal and A. K. Tyagi, *J. Phys. Chem. C*, 2009, **113**, 16954–16961.
3 L. Cheng, S. Zhu, W. Zheng and F. Huang, *Mater. Today Phys.*, 2020, **14**, 100244.
4 M. K. Hussen, F. B. Dejene and M. Tsega, *J. Mater. Sci.: Mater. Electron.*, 2019, **30**, 10191–10201.
5 C. He, H. Ji, Z. Huang, X. Zhang, Y. Liu, M. Fang, X. Wu and X. Min, *J. Rare Earths*, 2018, **36**, 931–938.
6 A. Fernández-Osorio, C. E. Rivera, A. Vázquez-Olmos and J. Chávez, *Dyes Pigm.*, 2015, **119**, 22–29.
7 I. Kamińska, K. Fronc, B. Sikora, K. Koper, R. Minikayev, W. Paszkowicz, K. Sobczak, T. Wojciechowski, M. Chwastyk, A. Reszka, B. J. Kowalski, P. Stepień and D. Elbaum, *RSC Adv.*, 2014, **4**, 56596–56604.
8 L. Cornu, M. Gaudon and V. Jubera, *J. Mater. Chem. C*, 2013, **1**, 5419–5428.
9 C. Ragupathi, L. John Kennedy and J. Judith Vijaya, *Adv. Powder Technol.*, 2014, **25**, 267–273.
10 A. A. Da Silva, A. S. Gonçalves, M. R. Davolosv and S. H. Santagneli, *J. Nanosci. Nanotechnol.*, 2008, **8**, 5690–5695.
11 D. Yang, G. Zhao, Q. Pan, M. Liang, Z. Ma, G. Dong, D. Chen and J. Qiu, *Mater. Express*, 2013, **3**, 210–216.
12 R. E. Rojas-Hernandez, L. F. Santos and R. M. Almeida, *J. Lumin.*, 2018, **197**, 180–186.
13 R. E. Rojas-Hernandez, F. Rubio-Marcos, A. Serrano, A. Del and J. F. Fernandez, *Sci. Rep.*, 2017, **7**, 1–9.
14 M. Bauch, K. Toma, M. Toma, Q. Zhang and J. Dostalek, *Plasmonics*, 2014, **9**, 781–799.
15 S. Sun, I. L. Rasskazov, P. S. Carney, T. Zhang and A. Moroz, *J. Phys. Chem. C*, 2020, **124**, 13365–13373.
16 V. Vargas, A. Sedova, S. Moscardini, L. Rocha and C. Falcony, *Ceram. Int.*, 2020, **46**(3), 3345–3352.
17 G. H. Dieke, *Spectra and Energy Levels of Rare Earth Ions in Crystals*, Interscience Publishers, 1968.
18 K. Lenczewska, R. Tomala and D. Hreniak, *Opt. Mater.*, 2017, **74**, 12–15.
19 A. Podhorodecki, M. Banski, J. Misiewicz, C. Lecerf, P. Marie, J. Cardin and X. Portier, *J. Appl. Phys.*, 2010, **108**(6), 063535.
20 X. Wang, L. Wang, Y. Luo, W. Wu, X. Tian, Q. Zhang and B. Chen, *J. Mater. Res.*, 2011, **26**, 1517–1523.
21 J. Xu, D. Murata, J. Ueda and S. Tanabe, *J. Mater. Chem. C*, 2016, **4**, 11096–11103.
22 H. E. Hoefdraad, *J. Inorg. Nucl. Chem.*, 1975, **37**, 1917–1921.
23 M. Yamaga, Y. Oda, H. Uno, K. Hasegawa, H. Ito and S. Mizuno, *Phys. Status Solidi C*, 2012, **9**, 2300–2303.
24 P. Samuel, T. Yanagitani, H. Yagi, H. Nakao, K. I. Ueda and S. M. Babu, *J. Alloys Compd.*, 2010, **507**, 475–478.
25 A. Vyas, C. P. Joshi and S. V. Moharil, *J. Alloys Compd.*, 2018, **763**, 159–163.
26 P. K. Tawalare, V. B. Bhatkar, S. K. Omanwar and S. V. Moharil, *J. Alloys Compd.*, 2019, **771**, 534–540.
27 C. K. Jørgensen, *Absorption Spectra and Chemical Bonding in Complexes*, 1962, vol. 12, pp. 146–172.
28 W. M. Mulwa, B. F. Dejene, M. O. Onani and C. N. M. Ouma, *J. Lumin.*, 2017, **184**, 7–16.
29 J. Xue, T. Wu, Y. Dai and Y. Xia, *Chem. Rev.*, 2019, **119**, 5298–5415.
30 S. Chen, J. V. John, A. McCarthy and J. Xie, *J. Mater. Chem. B*, 2020, **8**, 3733–3746.
31 D. Yang, G. Zhao, Q. Pan, M. Liang, Z. Ma, G. Dong, D. Chen and J. Qiu, *Mater. Express*, 2013, **3**, 210–216.
32 P. Moradipour, F. Dabirian and M. Moradipour, *Ceram. Int.*, 2020, **46**, 5566–5574.
33 H. M. Rietveld, *Acta Crystallogr.*, 1966, **20**, 508–513.
34 H. M. Rietveld, *J. Appl. Crystallogr.*, 1969, **2**, 65–71.
35 B. Ravel and M. Newville, *J. Synchrotron Radiat.*, 2005, **12**, 537–541.
36 J. R. Ferrar, K. Nakamoto and C. W. Brown, *Introductory Raman Spectroscopy*, Elsevier, 2003.
37 M. I. Aroyo, A. Kirov, C. Capillas, J. M. Perez-Mato and H. Wondratschek, *Acta Crystallogr., Sect. A: Found. Crystallogr.*, 2006, **A62**, 115–128.
38 M. I. Aroyo, J. M. Perez-Mato, C. Capillas, E. Kroumovo, S. Ivantchev, G. Madariaga, A. Kirov and H. Wondratschek, *Z. Kristallogr.*, 2006, **221**, 5–27.
39 M. I. Aroyo, J. M. Perez-Mato, D. Orobengoa, E. Tasci, G. de la Flor and A. Kirov, *Bulg. Chem. Commun.*, 2011, **43**, 183–197.
40 R. Cuscó, E. Alarcón-Lladó, J. Ibáñez, L. Artús, J. Jiménez, B. Wang and M. J. Callahan, *Phys. Rev. B: Condens. Matter Mater. Phys.*, 2007, **75**, 1–11.
41 Y. Liu, B. Cheng, K. K. Wang, G. P. Ling, J. Cai, C. L. Song and G. R. Han, *Solid State Commun.*, 2014, **178**, 16–22.
42 J. Cui and G. A. Hope, *J. Spectrosc.*, 2015, **2015**, 940172.
43 M. Guo, J. Lu, Y. Wu, Y. Wang and M. Luo, *Langmuir*, 2011, **27**, 3872–3877.
44 Z. D. Dohević-Mitrović, M. Grujić-Brojin, M. Ćepanović, Z. V. Popović, S. Boković, B. Matović, M. Zinkevich and F. Aldinger, *J. Phys.: Condens. Matter*, 2006, **18**(33), S2061.
45 S. López-Moreno, P. Rodríguez-Hernández, A. Muñoz, A. H. Romero, F. J. Manjón, D. Errandonea, E. Rusu and V. V. Ursaki, *Ann. Phys.*, 2011, **523**, 157–167.
46 V. D'Ippolito, G. B. Andreozzi, D. Bersani and P. P. Lottici, *J. Raman Spectrosc.*, 2015, **46**, 1255–1264.
47 J. Q. Brown, K. Vishwanath, G. M. Palmer and N. Ramanujam, *Curr. Opin. Biotechnol.*, 2009, **20**, 119–131.
48 N. Basavaraju, K. R. Priolkar, D. Gourier, S. K. Sharma, A. Bessière and B. Viana, *Phys. Chem. Chem. Phys.*, 2015, **17**, 1790–1799.
49 A. Bianconi, A. Marcelli, H. Dexpert, R. Karnatak, A. Kotani, T. Jo and J. Petiau, *Phys. Rev. B: Condens. Matter Mater. Phys.*, 1987, **35**, 806–812.
50 A. M. Shahin, F. Grandjean, G. J. Long and T. P. Schuman, *Chem. Mater.*, 2005, **17**, 315–321.
51 O. Niehaus, P. M. Abdala, J. F. Riecken, F. Winter, B. Chevalier and R. Pöttgen, *Z. Naturforsch., B: J. Chem. Sci.*, 2013, **68**, 960–970.

52 S. H. Overbury, D. R. Huntley, D. R. Mullins and G. N. Glavee, *Catal. Lett.*, 1998, **51**, 133–138.
53 F. Zhang, P. Wang, J. Koberstein, S. Khalid and S. W. Chan, *Surf. Sci.*, 2004, **563**, 74–82.
54 B. Joseph, A. Iadecola, M. Fratini, A. Bianconi, A. Marcelli and N. L. Saini, *J. Phys.: Condens. Matter*, 2009, **21**(43), 432201.
55 J. Cheng, S. Chu, W. Chu, W. Xu, J. Zhou, L. Zhang, H. Zhao, R. Liu, X. Chen, A. Marcelli and Z. Wu, *J. Synchrotron Radiat.*, 2011, **18**, 723–727.
56 P. Druska, U. Steinike and V. Šepelák, *J. Solid State Chem.*, 1999, **146**, 13–21.
57 S. S. Pitale, V. Kumar, I. M. Nagpure, O. M. Ntwaeaborwa and H. C. Swart, *Appl. Surf. Sci.*, 2011, **257**, 3298–3306.
58 B. R. Strohmeier, *Surf. Sci. Spectra*, 1994, **3**, 141–146.
59 D. A. Pawlak, K. Woźniak, Z. Frukacz, T. L. Barr, D. Fiorentino and S. Hardcastle, *J. Phys. Chem. B*, 1999, **103**, 3332–3336.
60 E. Bêche, P. Charvin, D. Perarnau, S. Abanades and G. Flamant, *Surf. Interface Anal.*, 2008, **40**, 264–267.
61 C. M. Sims, R. A. Maier, A. C. Johnston-Peck, J. M. Gorham, V. A. Hackley and B. C. Nelson, *Nanotechnology*, 2019, **30**(8), 085703.
62 K. I. Maslakov, Y. A. Teterin, A. J. Popel, A. Y. Teterin, K. E. Ivanov, S. N. Kalmykov, V. G. Petrov, P. K. Petrov and I. Farnan, *Appl. Surf. Sci.*, 2018, **448**, 154–162.
63 J. L. Suárez-Franco, M. García-Hipólito, M. Á. Surárez-Rosales, J. A. Fernández-Pedrero, O. Álvarez-Fregoso, J. A. Juárez-Islas and M. A. Álvarez-Pérez, *J. Nanomater.*, 2013, **2013**, 361249.

